

Minimizing L_1 over L_2 norms on the gradient

Chao Wang¹, Min Tao², Chen-Nee Chuah¹, James Nagy³, and Yifei Lou⁴

¹Department of Electrical and Computer Engineering, University of California Davis, Davis, CA 95616, USA

²Department of Mathematics, National Key Laboratory for Novel Software Technology, Nanjing University, Nanjing 210093, China

³Department of Mathematics, Emory University, Atlanta, GA 30322, USA

⁴Department of Mathematical Sciences, University of Texas at Dallas, Richardson, TX 75080, USA

E-mail: chaowang.hk@gmail.com, taom@nju.edu.cn, chuah@ucdavis.edu, jnagy@emory.edu, yifei.lou@utdallas.edu

Abstract. In this paper, we study the L_1/L_2 minimization on the gradient for imaging applications. Several recent works have demonstrated that L_1/L_2 is better than the L_1 norm when approximating the L_0 norm to promote sparsity. Consequently, we postulate that applying L_1/L_2 on the gradient is better than the classic total variation (the L_1 norm on the gradient) to enforce the sparsity of the image gradient. To verify our hypothesis, we consider a constrained formulation to reveal empirical evidence on the superiority of L_1/L_2 over L_1 when recovering piecewise constant signals from low-frequency measurements. Numerically, we design a specific splitting scheme, under which we can prove the subsequential convergence for the alternating direction method of multipliers (ADMM). Experimentally, we demonstrate visible improvements of L_1/L_2 over L_1 and other nonconvex regularizations for image recovery from low-frequency measurements and two medical applications of MRI and CT reconstruction. All the numerical results show the efficiency of our proposed approach.

Keywords: L_1/L_2 minimization, piecewise constant images, minimum separation, alternating direction method of multipliers

Submitted to: *Inverse Problems*

1. Introduction

Regularization methods play an important role in inverse problems to refine the solution space by prior knowledge and/or special structures. For example, the celebrated total variation (TV) [1] prefers piecewise constant images, while total generalized variation (TGV) [2] and fractional-order TV [3, 4] tend to preserve piecewise smoothness of an image. TV can be defined either isotropically or anisotropically. The anisotropic TV [5]

is equivalent to applying the L_1 norm on the image gradient. As the L_1 norm is often used to enforce a signal being *sparse*, one can interpret the TV regularization as to promote the sparsity of gradient vectors. In this paper, we aim at a series of advances in recovering sparse signals to analyze sparse gradient, which is specifically useful in imaging applications.

To find the sparsest signal, it is straightforward to minimize the L_0 norm (counting the number of nonzero elements), which is unfortunately NP-hard [6]. A popular approach involves the convex relaxation of using the L_1 norm to replace the ill-posed L_0 norm, with the equivalence between L_1 and L_0 for sparse signal recovery given in terms of restricted isometry property (RIP) [7]. However, Fan and Li [8] pointed out that the L_1 approach is biased towards large coefficients, and proposed to minimize a nonconvex regularization, called smoothly clipped absolute deviation (SCAD). Subsequently, various nonconvex functionals emerged such as minimax concave penalty (MCP) [9], capped L_1 [10, 11, 12], and transformed L_1 [13, 14, 15]. Following the literature on sparse signal recovery, there is a trend to apply a nonconvex regularization on the gradient to deal with images. For instance, Chartrand [16] discussed both the L_p norm with $0 < p < 1$ for sparse signals and L_p on the gradient for magnetic resonance imaging (MRI), while MCP on the gradient was examined in [17]. Motivated by the recent success of a scale-invariant functional L_1/L_2 [18, 19, 20], we focus on adapting it to promote sparse gradients for prototypical applications in image processing.

Despite their popular adoption to tackle inverse problems, gradient-based approaches lack theoretical guarantee on exact recovery, except for the RIP type of conditions [21, 22]. As RIP is NP-hard to verify [23], these conditions are impractical to analyze. We intend to borrow the analysis of a *super-resolution* problem, which refers to recovering a sparse signal from its low-frequency measurements. Candès and Fernandez-Granda [24] proved that if a signal has spikes (locations of nonzero elements) that are sufficiently separated, then the L_1 minimization yields an exact recovery for super-resolution. We innovatively design a certain type of piecewise constant signals that lead to well-separated spikes after taking the gradient. Using such signals, we empirically demonstrate that the TV minimization can find the desired solution under a similar separation condition as in [24]. We also illustrate that L_1/L_2 can deal with less separated spikes in gradient, and is better at preserving image contrast than L_1 . These empirical evidences show the superiority of L_1/L_2 over the classic TV regularization. To the best of our knowledge, it is the first time to relate the exact recovery of gradient-based methods to minimum separation and image contrast in a super-resolution problem.

Numerically, we consider the same splitting scheme used in an unconstrained formulation [25] to minimize the L_1/L_2 on the gradient, followed by the alternating direction method of multipliers (ADMM) [26]. We formulate the linear constraint using an indicator function, which is not strongly convex. As a result, the convergence analysis in the unconstrained model [25] is not directly applicable to our problem. We further utilize the property of indicator function as well as the optimality conditions for constrained optimization problems to establish the subsequential convergence analysis

of the proposed algorithm in the constrained model. As ADMM involves a subproblem that does not have a closed-form solution, we also provide the convergence analysis of solving the subproblem inexactly.

We present some algorithmic insights on computational efficiency of our proposed algorithm for nonconvex optimization. In particular, we show an additional box constraint not only prevents the solution from being stuck at local minima, but also stabilizes the algorithm. Furthermore, we discuss algorithmic behaviors on two types of applications: MRI and computed tomography (CT). For the MRI reconstruction, a subproblem in ADMM has a closed-form solution, while an iterative solver is required for CT. As the accuracy of the subproblem varies between MRI and CT, we shall alter internal settings of our algorithm accordingly. In summary, this paper relies on a constrained formulation to discuss theoretical and computational aspects of a nonconvex regularization for imaging problems. The major contributions are three-fold:

- (i) We reveal empirical evidences towards exact recovery of piecewise constant signals and demonstrate the superiority of L_1/L_2 on the gradient over TV.
- (ii) We establish subsequential convergence of the proposed algorithm with a relaxed solver for the subproblem.
- (iii) We conduct extensive experiments to characterize computational efficiency of our algorithm and discuss how internal settings can be customized to cater to specific imaging applications, such as MRI and limited-angle CT reconstruction. Numerical results highlight the superior performance of our approach over other gradient-based regularizations.

The rest of the paper is organized as follows. Section 2 defines the notations that will be used through the paper, and gives a brief review on the related works. The empirical evidences for TV’s exact recovery and advantages of the proposed model are given in Section 3. The numerical scheme is detailed in Section 4, followed by convergence analysis in Section 5. Section 6 presents three types of imaging applications: super-resolution, MRI and CT reconstruction problems. Finally, conclusions and future works are given in Section 7.

2. Preliminaries

We use a bold letter to denote a vector, a capital letter to denote a matrix or linear operator, and a calligraphic letter for a functional space. We use \odot to denote the component-wise multiplication of two vectors. When a function (e.g., sign, max, min) applies to a vector, it returns a vector with corresponding component-wise operation.

We adopt a discrete setting to describe the related models. Suppose a two-dimensional (2D) image is defined on an $m \times n$ Cartesian grid. By using a standard linear index, we can represent a 2D image as a vector, i.e., the $((i-1)m + j)$ -th component

denotes the intensity value at pixel (i, j) . We define a discrete gradient operator,

$$D\mathbf{u} := \begin{bmatrix} D_x \\ D_y \end{bmatrix} \mathbf{u}, \quad (1)$$

where D_x, D_y are the finite forward difference operator in the horizontal and vertical directions, respectively. We denote the Euclidean spaces by $\mathcal{X} := \mathbb{R}^{mn}, \mathcal{Y} := \mathbb{R}^{2mn}$, then $\mathbf{u} \in \mathcal{X}$ and $D\mathbf{u} \in \mathcal{Y}$. We can apply the standard norms, e.g., L_1, L_2 , on vectors \mathbf{u} and $D\mathbf{u}$. For example, the L_1 norm on the gradient, i.e., $\|D\mathbf{u}\|_1$, is the anisotropic TV regularization [5]. Throughout the paper, we use TV and “ L_1 on the gradient” interchangeably. Note that the isotropic TV [1] is the $L_{2,1}$ norm, i.e., $\|(D_x\mathbf{u}, D_y\mathbf{u})^T\|_{2,1}$, although Lou et al. [27] claimed to consider a weighted difference of anisotropic and isotropic TV based on the L_1 - L_2 functional [28, 29, 30, 31] (isotropic TV is not the L_2 norm on the gradient.)

We examine the L_1/L_2 penalty on the gradient in a constrained formulation,

$$\min_{\mathbf{u}} \frac{\|D\mathbf{u}\|_1}{\|D\mathbf{u}\|_2} \quad \text{s.t. } A\mathbf{u} = \mathbf{b}. \quad (2)$$

One way to solve for (2) involves the following equivalent form

$$\min_{\mathbf{u}, \mathbf{d}, \mathbf{h}} \frac{\|\mathbf{d}\|_1}{\|\mathbf{h}\|_2} \quad \text{s.t. } A\mathbf{u} = \mathbf{b}, \mathbf{d} = D\mathbf{u}, \mathbf{h} = D\mathbf{u}, \quad (3)$$

with two auxiliary variables \mathbf{d} and \mathbf{h} . For more details, please refer to [18] that presented a proof-of-concept example for MRI reconstruction. Since the splitting scheme (3) involves two block variables of \mathbf{u} and (\mathbf{d}, \mathbf{h}) , the existing ADMM convergence results [32, 33, 34] are not applicable. An alternative approach was discussed in our preliminary work [25] for an unconstrained minimization problem,

$$\min_{\mathbf{u}, \mathbf{h}} \frac{\|D\mathbf{u}\|_1}{\|\mathbf{h}\|_2} + \frac{\lambda}{2} \|A\mathbf{u} - \mathbf{b}\|_2^2 \quad \text{s.t. } \mathbf{h} = D\mathbf{u}, \quad (4)$$

where $\lambda > 0$ is a weighting parameter. By only introducing one variable \mathbf{h} , the new splitting scheme (4) can guarantee the ADMM framework with subsequential convergence.

In this paper, we incorporate the splitting scheme (4) to solve the constrained problem (2), which is crucial to reveal theoretical properties of the gradient-based regularizations for image reconstruction, as elaborated in Section 3. The constrained formulation indeed limits our experimental design in a noise-free fashion, but it helps us to draw conclusions solely on the model, ruling out the influence from other nuisances such as noises and tuning parameters. Our model (2) is parameter-free, while there is a parameter λ in the unconstrained problem (4).

3. Empirical studies

We aim to demonstrate the superiority of L_1/L_2 on the gradient over TV for a super-resolution problem [35], in which a sparse vector can be exactly recovered via the L_1 minimization. A mathematical model for *super-resolution* is expressed as

$$b_k = \frac{1}{\sqrt{N}} \sum_{j=0}^{N-1} u_j e^{-i2\pi kj/N}, \quad |k| \leq f_c, \quad (5)$$

where i is the imaginary unit, $\mathbf{u} \in \mathbb{R}^N$ is a vector to be recovered, and $\mathbf{b} \in \mathbb{C}^n$ consists of the given low frequency measurements with $n = 2f_c + 1 < N$. Recovering \mathbf{u} from \mathbf{b} is referred to as super-resolution in the sense that the underlying signal \mathbf{u} is defined on a fine grid with spacing $1/N$, while a direct inversion of n frequency data yields a signal defined on a coarser grid with spacing $1/n$. For simplicity, we use matrix notation to rewrite (5) as $\mathbf{b} = S_n F \mathbf{u}$, where S_n is a sampling matrix that collects the required low frequencies and F is the Fourier transform matrix. A sparse signal can be represented by $\mathbf{u} = \sum_{j \in T} c_j \mathbf{e}_j$, where \mathbf{e}_j is the j -th canonical basis in \mathbb{R}^N , T is the support set of \mathbf{u} , and $\{c_j\}$ are coefficients. Following the work of [35], the sparse spikes are required to be sufficiently separated to guarantee the exact recovery of the L_1 minimization. To make the paper self-contained, we provide the definition of minimum separation in Definition 1 and an exact recovery condition in Theorem 1.

Definition 1. (Minimum Separation [35]) For an index set $T \subset \{1, \dots, N\}$, the minimum separation (MS) of T is defined as the closest wrap-around distance between any two elements from T ,

$$\Delta(T) := \min_{(t, \tau) \in T: t \neq \tau} \min \{|t - \tau|, N - |t - \tau|\}. \quad (6)$$

Theorem 1. [35, Corollary 1.4] Let T be the support of \mathbf{u} . If the minimum separation of T obeys

$$\Delta(T) \geq \frac{1.87N}{f_c}, \quad (7)$$

then $\mathbf{u} \in \mathbb{R}^N$ is the unique solution to the constrained L_1 minimization problem,

$$\min_{\mathbf{u}} \|\mathbf{u}\|_1 \quad \text{s.t.} \quad S_n F \mathbf{u} = \mathbf{b}. \quad (8)$$

We empirically extend the analysis from sparse signals to sparse gradients. For this purpose, we construct a one-bar step function of length 100 with the first and the last s elements taking value 0, and the remaining elements equal to 1, as illustrated in Figure 1. The gradient of such signal is 2-sparse with MS to be $\min(2s, 100 - 2s)$ due to wrap-around distance. By setting $f_c = 2$, we only take $n = 5$ low frequency measurements, and reconstruct the signal by minimizing either L_1 or L_1/L_2 on the gradient. For simplicity, we adopt the CVX MATLAB toolbox [36] for solving the TV model,

$$\min_{\mathbf{u}} \|D\mathbf{u}\|_1 \quad \text{s.t.} \quad A\mathbf{u} = \mathbf{b}, \quad (9)$$

where we use $A = S_n F$ to be consistent with our setting (2). Note that the TV model (9) is parameter free, while we need to tune an algorithmic parameter for L_1/L_2 . Please refer to Section 4 for more details on the L_1/L_2 minimization, in which one subproblem can be solved by CVX, and Section 6.1 for sensitivity analysis on this parameter.

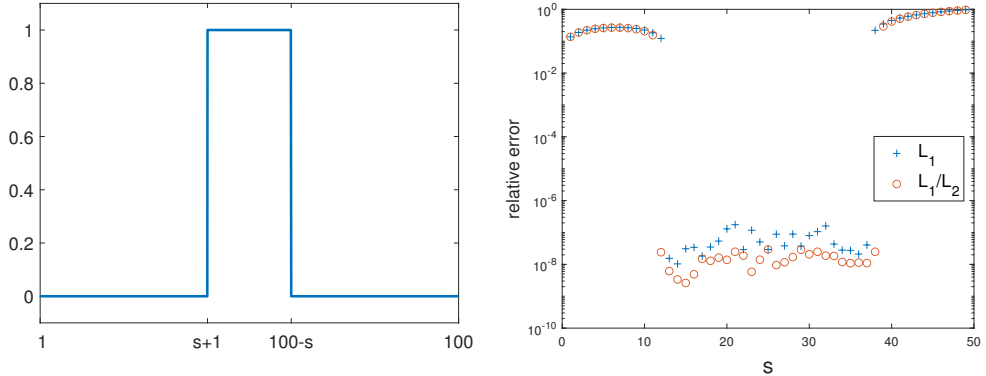


Figure 1. A general setting of a one-bar step function (left) and reconstruction errors with respect to s (right) by minimizing L_1 or L_1/L_2 on the gradient.

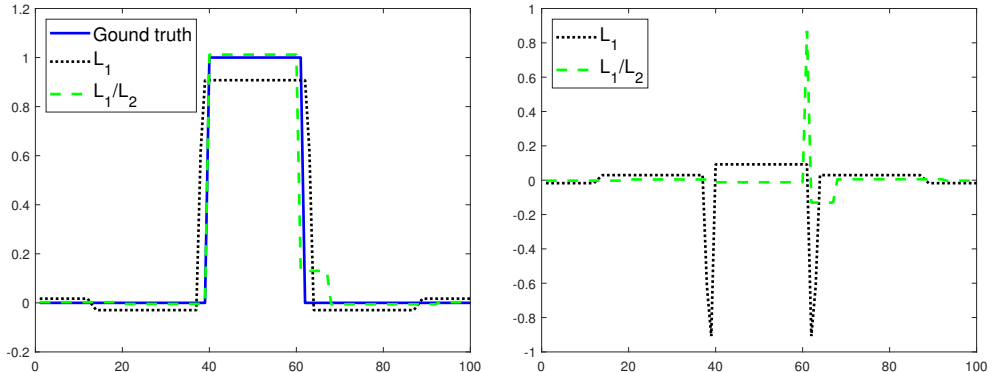


Figure 2. A particular one-bar example (left) where both L_1 and L_1/L_2 models fail to find the solution. The different plot (right) highlights that L_1 results in larger oscillations compared to L_1/L_2 .

By varying the value of s that changes MS of the spikes in gradient, we compute the relative errors between the reconstructed solutions and the ground-truth signals. If we define an exact recovery for its relative error smaller than 10^{-6} , we observe in Figure 1 that the exact recovery by L_1 occurs at $s \in [13, 37]$, which implies that MS is larger than or equal to 26. This phenomenon suggests that Theorem 1 might hold for sparse gradients by replacing the L_1 norm with the total variation. Figure 1 also shows the exact recovery by L_1/L_2 at $s \in [12, 38]$, meaning that L_1/L_2 can deal with less separated spikes than L_1 . Moreover, we further study the reconstruction results at $s = 39$, where both models fail to find the true sparse signal. The restored solutions by these two models as well as the different plots between restored and ground truth are displayed in Figure 2, showing that our ratio model has smaller relative errors than L_1 .

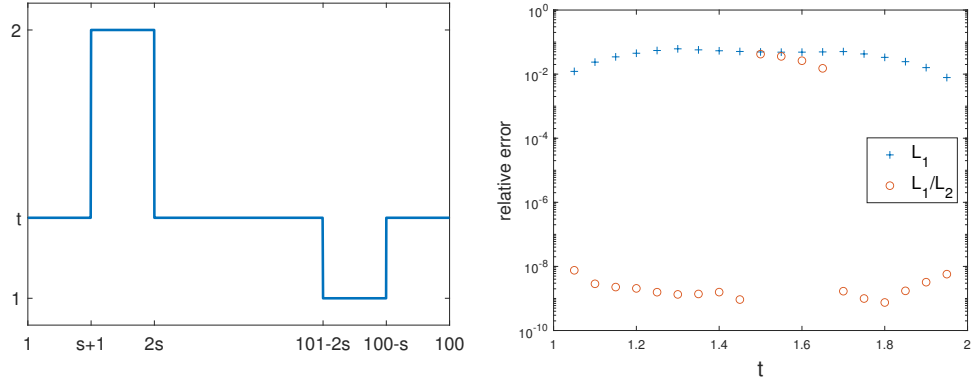


Figure 3. A general setting of a two-bar step function (left) and reconstruction errors with respect to t (right) by minimizing L_1 or L_1/L_2 on the gradient.

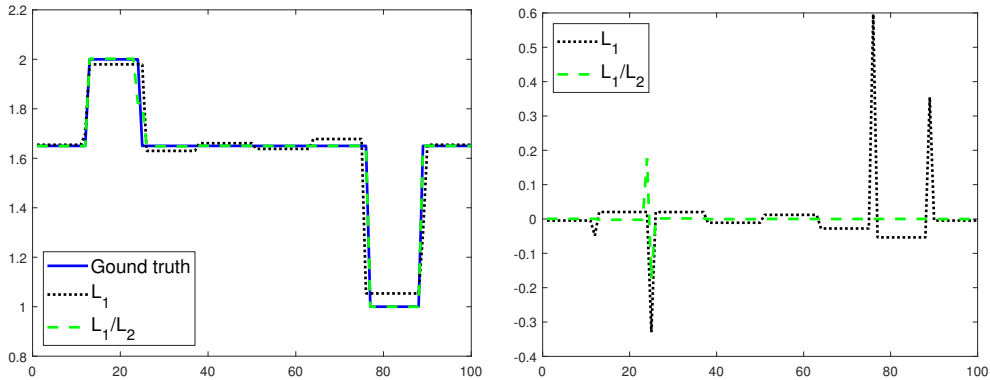


Figure 4. A particular two-bar example where both L_1 and L_1/L_2 models fail to find the solution. The different plot is shown on the right.

Figure 2 illustrates that the TV solution can not reach the top of the bar in the ground-truth, which is referred to as *loss-of-contrast*. Motivated by this well-known drawback of TV, we postulate that the signal contrast may affect the performance of L_1 and L_1/L_2 . To verify, we examine a two-bar step function, in which the contrast varies by the relative heights of the two bars. Following MATLAB's notation, we set $\mathbf{u}(s+1 : 2s) = 2$, $\mathbf{u}(\text{end} - 2s + 1 : \text{end}) = 1$, and the value of remaining elements uniformly as t ; see Figure 3 for a general setting. We fix $s = 12$, and vary the value of $t \in (1, 2)$ to generate signals with different intensity contrasts. Considering four spikes in the gradient, we set $f_c = 4$ or equivalently 9 low-frequency measurements to reconstruct the signal. The reconstruction errors are plotted in Figure 3, which shows that L_1 fails in all the cases, and L_1/L_2 can find the signals except for $t \in [1.5, 1.65]$. We further examine a particular case of $t = 1.65$ in Figure 4, where both models fail to get an exact recovery, but L_1/L_2 yields smaller oscillations than L_1 near the edges. Figures 3 and 4 demonstrate that L_1/L_2 is better at preserving image contrast than L_1 .

We verify that all the solutions of L_1 and L_1/L_2 satisfy the linear constraint $A\mathbf{u} = \mathbf{b}$ with high accuracy thanks for CVX. We further investigate when the L_1 approach fails,

and discover that it yields a solution that has a smaller L_1 norm compared to the L_1 norm of the ground-truth, which implies that L_1 is not sufficient to enforce gradient sparse. On the other hand, L_1/L_2 solutions often have higher objective value than the ground-truth, which calls for a better algorithm that can potentially find the ground-truth. We also want to point out that L_1/L_2 solutions depend on initial conditions. In Figure 1 and Figure 3, we present the smallest relative errors among 10 random vectors for initial values.

In summary, we devote some empirical evidences, showing that the loss-of-contrast artifact caused by L_1 can be mitigated by L_1/L_2 . The analysis also reveals a similar relationship between sparse gradient recovery and minimum separation as Theorem 1, which calls for a theoretical justification in the future.

4. The proposed approach

Starting from (2), we incorporate an additional box constraint in the model, i.e.,

$$\min_{\mathbf{u}} \frac{\|D\mathbf{u}\|_1}{\|D\mathbf{u}\|_2} \quad \text{s.t.} \quad A\mathbf{u} = \mathbf{b}, \quad \mathbf{u} \in [p, q]. \quad (10)$$

The notation $\mathbf{u} \in [p, q]$ means that every element of \mathbf{u} is bounded by $[p, q]$. The box constraint is reasonable for image processing applications [37, 38], since pixel values are usually bounded by $[0, 1]$ or $[0, 255]$. On the other hand, the box constraint is particularly helpful for the L_1/L_2 model to prevent its divergence [19].

We unify the no-box version (2) and the box constraint (10) into the following equivalent form

$$\min_{\mathbf{u}, \mathbf{h}} \frac{\|D\mathbf{u}\|_1}{\|\mathbf{h}\|_2} + \Pi_{A\mathbf{u}=\mathbf{b}}(\mathbf{u}) + c\Pi_{[p,q]}(\mathbf{u}) \quad \text{s.t.} \quad D\mathbf{u} = \mathbf{h}, \quad (11)$$

where $c \geq 0$ is a scalar to turn off the box constraint when setting zero. Here $\Pi_S(\mathbf{t})$ is the indicator function that forces \mathbf{t} to belong to a feasible set S , i.e.,

$$\Pi_S(\mathbf{t}) = \begin{cases} 0 & \text{if } \mathbf{t} \in S \\ +\infty & \text{otherwise.} \end{cases} \quad (12)$$

The augmented Lagrangian function corresponding to (11) can be expressed as,

$$\mathcal{L}(\mathbf{u}, \mathbf{h}; \mathbf{g}) = \frac{\|D\mathbf{u}\|_1}{\|\mathbf{h}\|_2} + \Pi_{A\mathbf{u}=\mathbf{b}}(\mathbf{u}) + c\Pi_{[p,q]}(\mathbf{u}) + \langle \rho\mathbf{g}, D\mathbf{u} - \mathbf{h} \rangle + \frac{\rho}{2} \|D\mathbf{u} - \mathbf{h}\|_2^2, \quad (13)$$

where \mathbf{g} is a dual variable and ρ is a positive parameter. Then ADMM iterates as follows,

$$\begin{cases} \mathbf{u}^{(k+1)} = \arg \min_{\mathbf{u}} \mathcal{L}(\mathbf{u}, \mathbf{h}^{(k)}; \mathbf{g}^{(k)}) \\ \mathbf{h}^{(k+1)} = \arg \min_{\mathbf{h}} \mathcal{L}(\mathbf{u}^{(k+1)}, \mathbf{h}; \mathbf{g}^{(k)}) \\ \mathbf{g}^{(k+1)} = \mathbf{g}^{(k)} + D\mathbf{u}^{(k+1)} - \mathbf{h}^{(k+1)}. \end{cases} \quad (14)$$

The update for \mathbf{h} is the same as in [18], which has a closed-form solution of

$$\mathbf{h}^{(k+1)} = \begin{cases} \tau^{(k)}(D\mathbf{u}^{(k+1)} + \mathbf{g}^{(k)}) & \text{if } D\mathbf{u}^{(k+1)} + \mathbf{g}^{(k)} \neq \mathbf{0} \\ \mathbf{r}^{(k)} & \text{otherwise,} \end{cases} \quad (15)$$

where $\mathbf{r}^{(k)}$ is a random vector with the L_2 norm being $\sqrt[3]{\frac{\|D\mathbf{u}^{(k+1)}\|_1}{\rho}}$ and $\tau^{(k)} = \frac{1}{3} + \frac{1}{3}(\xi^{(k)} + \frac{1}{\xi^{(k)}})$ for

$$\xi^{(k)} = \sqrt[3]{\frac{27\eta^{(k)} + 2 + \sqrt{(27\eta^{(k)} + 2)^2 - 4}}{2}} \quad \text{and} \quad \eta^{(k)} = \frac{\|D\mathbf{u}^{(k+1)}\|_1}{\rho\|D\mathbf{u}^{(k+1)} + \mathbf{g}^{(k)}\|_2^3}.$$

We elaborate on the \mathbf{u} -subproblem in (14) with the box constraint, i.e.,

$$\mathbf{u}^{(k+1)} = \arg \min_{\mathbf{u}} \frac{\|D\mathbf{u}\|_1}{\|\mathbf{h}^{(k)}\|_2} + \frac{\rho}{2}\|D\mathbf{u} - \mathbf{h}^{(k)} + \mathbf{g}^{(k)}\|_2^2 \quad \text{s.t.} \quad A\mathbf{u} = \mathbf{b}, \mathbf{u} \in [p, q]. \quad (16)$$

The no-box version can follow similarly. To solve for (16), we introduce two variables, \mathbf{v} for the box constraint and \mathbf{d} for the gradient, thus getting

$$\min_{\mathbf{u}, \mathbf{d}, \mathbf{v}} \frac{\|\mathbf{d}\|_1}{\|\mathbf{h}^{(k)}\|_2} + \frac{\rho}{2}\|D\mathbf{u} - \mathbf{h}^{(k)} + \mathbf{g}^{(k)}\|_2^2 + \Pi_{[p, q]}(\mathbf{v}) \quad \text{s.t.} \quad \mathbf{u} = \mathbf{v}, D\mathbf{u} = \mathbf{d}, A\mathbf{u} = \mathbf{b}. \quad (17)$$

The augmented Lagrangian function corresponding to (17) becomes

$$\begin{aligned} \mathcal{L}^{(k)}(\mathbf{u}, \mathbf{d}, \mathbf{v}; \mathbf{w}, \mathbf{y}, \mathbf{z}) = & \frac{\|\mathbf{d}\|_1}{\|\mathbf{h}^{(k)}\|_2} + \frac{\rho}{2}\|D\mathbf{u} - \mathbf{h}^{(k)} + \mathbf{g}^{(k)}\|_2^2 + \Pi_{[c, d]}(\mathbf{v}) \\ & + \langle \beta \mathbf{w}, \mathbf{u} - \mathbf{v} \rangle + \frac{\beta}{2}\|\mathbf{u} - \mathbf{v}\|_2^2 \\ & + \langle \gamma \mathbf{y}, D\mathbf{u} - \mathbf{d} \rangle + \frac{\gamma}{2}\|D\mathbf{u} - \mathbf{d}\|_2^2 \\ & + \langle \lambda \mathbf{z}, A\mathbf{u} - \mathbf{b} \rangle + \frac{\lambda}{2}\|A\mathbf{u} - \mathbf{b}\|_2^2, \end{aligned} \quad (18)$$

where $\mathbf{w}, \mathbf{y}, \mathbf{z}$ are dual variables and β, γ, λ are positive parameters. Here we have k in the superscript of \mathcal{L} to indicate that it is the Lagrangian for the \mathbf{u} -subproblem in (14) at the k -th iteration. The ADMM framework to minimize (17) leads to

$$\begin{cases} \mathbf{u}_{j+1} = \arg \min_{\mathbf{u}} \mathcal{L}^{(k)}(\mathbf{u}, \mathbf{d}_j, \mathbf{v}_j; \mathbf{w}_j, \mathbf{y}_j, \mathbf{z}_j) \\ \mathbf{d}_{j+1} = \arg \min_{\mathbf{d}} \mathcal{L}^{(k)}(\mathbf{u}_{j+1}, \mathbf{d}, \mathbf{v}_j; \mathbf{w}_j, \mathbf{y}_j, \mathbf{z}_j) \\ \mathbf{v}_{j+1} = \arg \min_{\mathbf{v}} \mathcal{L}^{(k)}(\mathbf{u}_{j+1}, \mathbf{d}_{j+1}, \mathbf{v}; \mathbf{w}_j, \mathbf{y}_j, \mathbf{z}_j) \\ \mathbf{w}_{j+1} = \mathbf{w}_j + \mathbf{u}_{j+1} - \mathbf{v}_{j+1} \\ \mathbf{y}_{j+1} = \mathbf{y}_j + D\mathbf{u}_{j+1} - \mathbf{d}_{j+1} \\ \mathbf{z}_{j+1} = \mathbf{z}_j + A\mathbf{u}_{j+1} - \mathbf{b}, \end{cases} \quad (19)$$

where the subscript j represents the inner loop index, as opposed to the superscript k for outer iterations in (14). By taking derivative of $\mathcal{L}^{(k)}$ with respect to \mathbf{u} , we obtain a closed-form solution given by

$$\begin{aligned} \mathbf{u}_{j+1} = & \left(\lambda A^T A + (\rho + \gamma) D^T D + \beta I \right)^{-1} \left(\lambda A^T (\mathbf{b} - \mathbf{z}_j) \right. \\ & \left. + \gamma D^T (\mathbf{d}_j - \mathbf{y}_j) + \rho D^T (\mathbf{h}^{(k)} - \mathbf{g}^{(k)}) + \beta (\mathbf{v}_j - \mathbf{w}_j) \right), \end{aligned} \quad (20)$$

where I stands for the identity matrix. When the matrix A involves frequency measurements, e.g. in super-resolution and MRI reconstruction, the update in (20) can be implemented efficiently by the fast Fourier transform (FFT). For a general system matrix A , we adopt the conjugate gradient descent iterations [39] to solve for (20).

The \mathbf{d} -subproblem in (19) also has a closed-form solution, i.e.,

$$\mathbf{d}_{j+1} = \mathbf{shrink} \left(D\mathbf{u}_{j+1} + \mathbf{y}_j, \frac{1}{\gamma \|\mathbf{h}^{(k)}\|_2} \right), \quad (21)$$

where $\mathbf{shrink}(\mathbf{x}, \mu) = \text{sign}(\mathbf{x}) \odot \max \{|\mathbf{x}| - \mu, 0\}$. We update \mathbf{v} by a projection onto the $[p, q]$ -box constraint, which is given by

$$\mathbf{v}_{j+1} = \min \{ \max \{\mathbf{u}_{j+1} + \mathbf{w}_j, p\}, q \}.$$

For the no-box version, i.e., $c = 0$ in (13), we only need to remove the box constraint in the \mathbf{u} -subproblem (16). Algorithmically, we can simply set $\mathbf{v} = \mathbf{w} = \mathbf{0}$, and do not update them during iterations. For 1D super-resolution problem discussed in Section 3, we do not consider the box constraint and use the CVX toolbox to solve for the \mathbf{u} -subproblem. Note that we need to tune the parameter ρ for the L_1/L_2 model; please refer to Section 6.1 for sensitive analysis on ρ .

In summary, we present a unified algorithm to minimize the L_1/L_2 on the gradient subject to a linear system with or without the box constraint in Algorithm 1. If we only run one iteration of the \mathbf{u} -subproblem (19), the overall ADMM iteration (14) is equivalent to the previous approach [18]. If the \mathbf{u} -subproblem can be solved within a certain accuracy to the optimal solution, the convergence can be guaranteed; see Section 5.

5. Convergence analysis

We intend to establish the convergence of Algorithm 1 with the box constraint, which is extensively tested in the experiments. Since our ADMM framework (14) share the same structure with the unconstrained formulation, we adapt some analysis in [25] to prove the subsequential convergence for the proposed model (10). For example, we make the same assumption as in [25],

Assumption 1. $\mathcal{N}(D) \cap \mathcal{N}(A) = \{\mathbf{0}\}$, where \mathcal{N} denotes the null space and D is defined in (1). In addition, the norm of $\{\mathbf{h}^{(k)}\}$ generated by (14) has a lower bound, i.e., there exist a positive constant ϵ such that $\|\mathbf{h}^{(k)}\|_2 \geq \epsilon, \forall k$.

But unlike the unconstrained model, the strongly convexity of $\mathcal{L}(\mathbf{u}, \mathbf{h}, \mathbf{g})$ with respect to \mathbf{u} does not hold due to the indicator function $\Pi_{A\mathbf{u}=\mathbf{b}}(\mathbf{u})$. Besides, we have additional dual variable \mathbf{w} which is not in the unconstrained model. To avoid redundancies to [25], we focus on the different strategies to the unconstrained case, such as optimality conditions and subgradient of the indicator function, when proving convergence for the constrained problem, e.g., in Lemmas 1-2 and Theorem 2. In

Algorithm 1 The L_1/L_2 minimization on the gradient

```

1: Input: a linear operator  $A$ , observed data  $\mathbf{b}$ , and a bound  $[p, q]$  for the original image
2: Parameters:  $\rho, \lambda, \gamma, \beta$ , kMax, jMax, and  $\epsilon \in \mathbb{R}$ 
3: Initialize:  $\mathbf{h}, \mathbf{d}, \mathbf{g}, \mathbf{v}, \mathbf{w}, \mathbf{y}, \mathbf{z} = \mathbf{0}$ , and  $k, j = 0$ 
4: while  $k < \text{kMax}$  or  $\|\mathbf{u}^{(k)} - \mathbf{u}^{(k-1)}\|_2 / \|\mathbf{u}^{(k)}\|_2 > \epsilon$  do
5:   while  $j < \text{jMax}$  or  $\|\mathbf{u}_j - \mathbf{u}_{j-1}\|_2 / \|\mathbf{u}_j\|_2 > \epsilon$  do
6:      $\mathbf{u}_{j+1} = (\lambda A^T A + (\rho + \gamma) D^T D + \beta I)^{-1} (\lambda A^T (\mathbf{b} - \mathbf{z}_j) + \gamma D^T (\mathbf{d}_j - \mathbf{y}_j)$ 
       $+ \rho D^T (\mathbf{h}^{(k)} - \mathbf{g}^{(k)}) + \beta (\mathbf{v}_j - \mathbf{w}_j))$ 
7:      $\mathbf{d}_{j+1} = \text{shrink} \left( D\mathbf{u}_{j+1} + \mathbf{y}_j, \frac{1}{\gamma \|\mathbf{h}^{(k)}\|_2} \right)$ 
8:     
$$\begin{cases} \mathbf{v}_{j+1} = \min \{ \max \{ \mathbf{u}_{j+1} + \mathbf{w}_j, p \}, q \} & \text{for box} \\ \mathbf{w}_{j+1} = \mathbf{w}_j + \mathbf{u}_{j+1} - \mathbf{v}_{j+1} \end{cases}$$

9:      $\mathbf{y}_{j+1} = \mathbf{y}_j + D\mathbf{u}_{j+1} - \mathbf{d}_{j+1}$ 
10:     $\mathbf{z}_{j+1} = \mathbf{z}_j + A\mathbf{u}_{j+1} - \mathbf{b}$ 
11:     $j = j + 1$ 
12:  end while
13:  return  $\mathbf{u}^{(k+1)} = \mathbf{u}_j$ 
14:   $\mathbf{h}^{(k+1)} = \begin{cases} \tau^{(k)} (D\mathbf{u}^{(k+1)} + \mathbf{g}^{(k)}) & D\mathbf{u}^{(k+1)} + \mathbf{g}^{(k)} \neq 0 \\ \mathbf{r}^{(k)} & \text{otherwise} \end{cases}$ 
15:   $\mathbf{g}^{(k+1)} = \mathbf{g}^{(k)} + D\mathbf{u}^{(k+1)} - \mathbf{h}^{(k+1)}$ 
16:   $k = k + 1$  and  $j = 0$ 
17: end while
18: return  $\mathbf{u}^* = \mathbf{u}^{(k)}$ 

```

addition, we include a convergence result in Theorem 3 when the \mathbf{u} -subproblem in (14) can be solved inexactly. The proof follows directly from [25, Theorem 4.7], thus omitted.

Lemma 1. (sufficient descent) Under Assumption 1, the sequence $\{\mathbf{u}^{(k)}, \mathbf{h}^{(k)}, \mathbf{g}^{(k)}\}$ generated by (14) satisfies

$$\mathcal{L}(\mathbf{u}^{(k+1)}, \mathbf{h}^{(k+1)}; \mathbf{g}^{(k+1)}) \leq \mathcal{L}(\mathbf{u}^{(k)}, \mathbf{h}^{(k)}; \mathbf{g}^{(k)}) - c_1 \|\mathbf{u}^{(k+1)} - \mathbf{u}^{(k)}\|_2^2 - c_2 \|\mathbf{h}^{(k+1)} - \mathbf{h}^{(k)}\|_2^2, \quad (22)$$

where c_1 and c_2 are two positive constants for a sufficiently large ρ .

Proof. Denote σ as the smallest eigenvalue of the matrix $A^T A + D^T D$. We show σ is strictly positive. If $\sigma = 0$, there exists a vector \mathbf{x} such that $\mathbf{x}^T (A^T A + D^T D) \mathbf{x} = 0$. It is straightforward that $\mathbf{x}^T A^T A \mathbf{x} \geq 0$ and $\mathbf{x}^T D^T D \mathbf{x} \geq 0$, so one shall have $\mathbf{x}^T A^T A \mathbf{x} = 0$ and $\mathbf{x}^T D^T D \mathbf{x} = 0$, which contradicts $\mathcal{N}(D) \cap \mathcal{N}(A) = \{\mathbf{0}\}$ in Assumption 1. Therefore, there exists a positive $\sigma > 0$ such that

$$\mathbf{v}^T (A^T A + D^T D) \mathbf{v} \geq \sigma \|\mathbf{v}\|_2^2, \quad \forall \mathbf{v}.$$

By letting $\mathbf{v} = \mathbf{u}^{(k+1)} - \mathbf{u}^{(k)}$ and using $A\mathbf{u}^{(k+1)} = A\mathbf{u}^{(k)} = \mathbf{b}$, we have

$$\|D(\mathbf{u}^{(k+1)} - \mathbf{u}^{(k)})\|_2^2 \geq \sigma \|\mathbf{u}^{(k+1)} - \mathbf{u}^{(k)}\|_2^2. \quad (23)$$

We define $h := \|\mathbf{h}^{(k)}\|_2$, and express the \mathbf{u} -subproblem in (14) equivalently as

$$\begin{aligned} \mathbf{u}^{(k+1)} &= \arg \min_{\mathbf{u}} \frac{\|D\mathbf{u}\|_1}{h} + \frac{\rho}{2} \|D\mathbf{u} - \mathbf{h}^{(k)} + \mathbf{g}^{(k)}\|_2^2 \\ \text{s.t. } & A\mathbf{u} = \mathbf{b}, p - \mathbf{u} \leq \mathbf{0}, \text{ and } \mathbf{u} - q \leq \mathbf{0}. \end{aligned}$$

The optimality conditions state that $A\mathbf{u}^{(k+1)} = \mathbf{b}$ and there exist three sets of vectors \mathbf{w}_i , ($i = 1, 2, 3$) such that

$$\mathbf{0} \in \frac{\mathbf{p}^{(k+1)}}{h} + \rho D^T(D\mathbf{u}^{(k+1)} - \mathbf{h}^{(k)} + \mathbf{g}^{(k)}) + A^T\mathbf{w}_1 - \mathbf{w}_2 + \mathbf{w}_3, \quad (24)$$

with $\mathbf{p}^{(k+1)} \in \partial\|D\mathbf{u}^{(k+1)}\|_1$. By the complementary slackness, we have $\mathbf{w}_2, \mathbf{w}_3 \geq \mathbf{0}$ and

$$(p - \mathbf{u}^{(k+1)}) \odot \mathbf{w}_2 = (\mathbf{u}^{(k+1)} - q) \odot \mathbf{w}_3 = \mathbf{0}, \quad (25)$$

which also holds for $\mathbf{u}^{(k)}$. Using the definition of subgradient and (24), we obtain that

$$\begin{aligned} & \mathcal{L}(\mathbf{u}^{(k+1)}, \mathbf{h}^{(k)}; \mathbf{g}^{(k)}) - \mathcal{L}(\mathbf{u}^{(k)}, \mathbf{h}^{(k)}; \mathbf{g}^{(k)}) \\ & \leq \left\langle \frac{\mathbf{p}^{(k+1)}}{h}, \mathbf{u}^{(k+1)} - \mathbf{u}^{(k)} \right\rangle + \frac{\rho}{2} \|D\mathbf{u}^{(k+1)} - \mathbf{g}\|_2^2 - \frac{\rho}{2} \|D\mathbf{u}^{(k)} - \mathbf{g}\|_2^2 \\ & = - \langle \mathbf{w}_1, A\mathbf{u}^{(k+1)} - A\mathbf{u}^{(k)} \rangle + \langle \mathbf{w}_2, \mathbf{u}^{(k+1)} - \mathbf{u}^{(k)} \rangle - \langle \mathbf{w}_3, \mathbf{u}^{(k+1)} - A\mathbf{u}^{(k)} \rangle \\ & \quad - \rho \langle D\mathbf{u}^{(k+1)} - \mathbf{g}, D\mathbf{u}^{(k+1)} - D\mathbf{u}^{(k)} \rangle + \frac{\rho}{2} \|D\mathbf{u}^{(k+1)} - \mathbf{g}\|_2^2 - \frac{\rho}{2} \|D\mathbf{u}^{(k)} - \mathbf{g}\|_2^2 \\ & = - \frac{\rho}{2} \|D\mathbf{u}^{(k+1)} - D\mathbf{u}^{(k)}\|_2^2 \leq - \frac{\sigma\rho}{2} \|\mathbf{u}^{(k+1)} - \mathbf{u}^{(k)}\|_2^2, \end{aligned}$$

where we use (23), $A\mathbf{u}^{(k+1)} = A\mathbf{u}^{(k)} = \mathbf{b}$, and (25) for $\mathbf{u}^{(k)}$ and $\mathbf{u}^{(k+1)}$. The bounds of $\mathcal{L}(\mathbf{u}^{(k+1)}, \mathbf{h}^{(k+1)}; \mathbf{g}^{(k)}) - \mathcal{L}(\mathbf{u}^{(k+1)}, \mathbf{h}^{(k)}; \mathbf{g}^{(k)})$ and $\mathcal{L}(\mathbf{u}^{(k+1)}, \mathbf{h}^{(k+1)}; \mathbf{g}^{(k+1)}) - \mathcal{L}(\mathbf{u}^{(k+1)}, \mathbf{h}^{(k+1)}; \mathbf{g}^{(k)})$ exactly follow [25, Lemma 4.3] for the unconstrained formulation, which has the same ADMM framework (14) used in this paper, and hence we omit the rest of the proof. \square

Lemma 2. (subgradient bound) *Under Assumption 1, there exists a vector $\boldsymbol{\eta}^{(k+1)} \in \partial\mathcal{L}(\mathbf{u}^{(k+1)}, \mathbf{h}^{(k+1)}; \mathbf{g}^{(k+1)})$ and a constant $\gamma > 0$ such that*

$$\|\boldsymbol{\eta}^{(k+1)}\|_2^2 \leq \gamma (\|\mathbf{h}^{(k+1)} - \mathbf{h}^{(k)}\|_2^2 + \|\mathbf{g}^{(k+1)} - \mathbf{g}^{(k)}\|_2^2). \quad (26)$$

Proof. We define

$$\boldsymbol{\eta}_1^{(k+1)} := \frac{\mathbf{p}^{(k+1)}}{\|\mathbf{h}^{(k+1)}\|_2} + A^T\mathbf{w}_1 - \mathbf{w}_2 + \mathbf{w}_3 + \rho D^T(D\mathbf{u}^{(k+1)} - \mathbf{h}^{(k+1)} + \mathbf{g}^{(k+1)}).$$

Clearly by the subgradient definition, we can prove that $A^T\mathbf{w}_1 \in \partial\Pi_{A\mathbf{u}=\mathbf{b}}(\mathbf{u}^{(k+1)})$ and $\mathbf{w}_3 - \mathbf{w}_2 \in \partial\Pi_{[p,q]}(\mathbf{u}^{(k+1)})$, which implies that $\boldsymbol{\eta}_1^{(k+1)} \in \partial_u \mathcal{L}(\mathbf{u}^{(k+1)}, \mathbf{h}^{(k+1)}, \mathbf{g}^{(k+1)})$. Combining the definition of $\boldsymbol{\eta}_1^{(k+1)}$ with (24) leads to

$$\boldsymbol{\eta}_1^{(k+1)} = -\frac{\mathbf{p}^{(k+1)}}{\|\mathbf{h}^{(k)}\|_2} + \frac{\mathbf{p}^{(k+1)}}{\|\mathbf{h}^{(k+1)}\|_2} + \rho D^T(\mathbf{h}^{(k)} - \mathbf{h}^{(k+1)}) + \rho D^T(\mathbf{g}^{(k+1)} - \mathbf{g}^{(k)}),$$

which contributes an upper bound of $\|\boldsymbol{\eta}_1^{(k+1)}\|_2$ based on $\|\mathbf{h}^{(k+1)} - \mathbf{h}^{(k)}\|_2$ and $\|\mathbf{g}^{(k+1)} - \mathbf{g}^{(k)}\|_2$. We can also define $\boldsymbol{\eta}_2^{(k+1)}, \boldsymbol{\eta}_3^{(k+1)}$ such that

$$\begin{aligned}\boldsymbol{\eta}_2^{(k+1)} &\in \partial_{\mathbf{h}} \mathcal{L}(\mathbf{u}^{(k+1)}, \mathbf{h}^{(k+1)}, \mathbf{g}^{(k+1)}) \\ \boldsymbol{\eta}_3^{(k+1)} &\in \partial_{\mathbf{g}} \mathcal{L}(\mathbf{u}^{(k+1)}, \mathbf{h}^{(k+1)}, \mathbf{g}^{(k+1)}),\end{aligned}$$

and estimate the upper bounds of $\|\boldsymbol{\eta}_2^{(k+1)}\|_2$ and $\|\boldsymbol{\eta}_3^{(k+1)}\|_2$. The remaining proof is the same as in [25, Lemma 4.4]. \square

Theorem 2. (subsequential convergence) *Under Assumption 1 and a sufficiently large ρ , the sequence $\{\mathbf{u}^{(k)}, \mathbf{h}^{(k)}\}$ generated by (14) always has a subsequence convergent to a critical point of (11).*

Proof. Since $\mathbf{u}^{(k)}$ is bounded by $[p, q]$, then $\|D\mathbf{u}^{(k)}\|_1$ is bounded; i.e., there exists a constant $M > 0$ such that $\|D\mathbf{u}^{(k)}\|_1 \leq M$. The optimality condition of the \mathbf{h} -subproblem in (14) leads to

$$-\frac{a^{(k+1)}}{\|\mathbf{h}^{(k+1)}\|^3} \mathbf{h}^{(k+1)} + \rho (\mathbf{h}^{(k+1)} - D\mathbf{u}^{(k+1)} - \mathbf{g}^{(k)}) = \mathbf{0}, \quad (27)$$

where $a^{(k)} := \|D\mathbf{u}^{(k)}\|_1$. Using the dual update $-\mathbf{g}^{(k+1)} = \mathbf{h}^{(k+1)} - D\mathbf{u}^{(k+1)} - \mathbf{g}^{(k)}$, we have

$$\mathbf{g}^{(k+1)} = -\frac{a^{(k+1)}}{\rho} \frac{\mathbf{h}^{(k+1)}}{\|\mathbf{h}^{(k+1)}\|^3}. \quad (28)$$

Due to $\|\mathbf{h}^{(k)}\|_2 \geq \epsilon$ in Assumption 1, we get

$$\|\mathbf{g}^{(k)}\|_2 = \left\| \frac{a^{(k+1)}}{\rho} \frac{\mathbf{h}^{(k)}}{\|\mathbf{h}^{(k)}\|^3} \right\|_2 \leq \frac{M}{\rho\epsilon^2},$$

which implies the boundedness of $\{\mathbf{g}^{(k)}\}$. It follows from the \mathbf{h} -update (15) that $\{\mathbf{h}^{(k)}\}$ is also bounded. Therefore, the Bolzano-Weierstrass Theorem guarantees that the sequence $\{\mathbf{u}^{(k)}, \mathbf{h}^{(k)}, \mathbf{g}^{(k)}\}$ has a convergent subsequence, denoted by $(\mathbf{u}^{(k_j)}, \mathbf{h}^{(k_j)}, \mathbf{g}^{(k_j)}) \rightarrow (\mathbf{u}^*, \mathbf{h}^*, \mathbf{g}^*)$, as $k_j \rightarrow \infty$. In addition, we can estimate that

$$\begin{aligned}\mathcal{L}(\mathbf{u}^{(k)}, \mathbf{h}^{(k)}; \mathbf{g}^{(k)}) &= \frac{\|D\mathbf{u}^{(k)}\|_1}{\|\mathbf{h}^{(k)}\|_2} + \Pi_{A\mathbf{u}=\mathbf{b}}(\mathbf{u}^{(k)}) + \frac{\rho}{2} \|\mathbf{h}^{(k)} - \nabla \mathbf{u}^{(k)} - \mathbf{g}\|_2^2 - \frac{\rho}{2} \|\mathbf{g}^{(k)}\|_2^2 \\ &\geq \frac{\|D\mathbf{u}^{(k)}\|_1}{\|\mathbf{h}^{(k)}\|_2} - \frac{\|D\mathbf{u}^{(k)}\|_1^2}{\rho\epsilon^4},\end{aligned}$$

which gives a lower bound of \mathcal{L} owing to the boundedness of $\mathbf{u}^{(k)}$ and $\mathbf{h}^{(k)}$. It further follows from Lemma 1 that $\mathcal{L}(\mathbf{u}^{(k)}, \mathbf{h}^{(k)}, \mathbf{g}^{(k)})$ converges due to its monotonic decreasing.

We then sum the inequality (22) from $k = 0$ to K , thus getting

$$\begin{aligned}\mathcal{L}(\mathbf{u}^{(K+1)}, \mathbf{h}^{(K+1)}; \mathbf{g}^{(k+1)}) &\leq \mathcal{L}(\mathbf{u}^{(0)}, \mathbf{h}^{(0)}; \mathbf{g}^{(0)}) - c_1 \sum_{k=0}^K \|\mathbf{u}^{(k+1)} - \mathbf{u}^{(k)}\|_2^2 - c_2 \sum_{k=0}^K \|\mathbf{h}^{(k+1)} - \mathbf{h}^{(k)}\|_2^2.\end{aligned}$$

Let $K \rightarrow \infty$, we have both summations of $\sum_{k=0}^{\infty} \|\mathbf{u}^{(k+1)} - \mathbf{u}^{(k)}\|_2^2$ and $\sum_{k=0}^{\infty} \|\mathbf{h}^{(k+1)} - \mathbf{h}^{(k)}\|_2^2$ are finite, indicating that $\mathbf{u}^{(k)} - \mathbf{u}^{(k+1)} \rightarrow 0$, $\mathbf{h}^{(k)} - \mathbf{h}^{(k+1)} \rightarrow 0$. Then by [25, Lemma 4.2], we get $\mathbf{g}^{(k)} - \mathbf{g}^{(k+1)} \rightarrow 0$. By $(\mathbf{u}^{(k_j)}, \mathbf{h}^{(k_j)}, \mathbf{g}^{(k_j)}) \rightarrow (\mathbf{u}^*, \mathbf{h}^*, \mathbf{g}^*)$, we have $(\mathbf{u}^{(k_j+1)}, \mathbf{h}^{(k_j+1)}, \mathbf{g}^{(k_j+1)}) \rightarrow (\mathbf{u}^*, \mathbf{h}^*, \mathbf{g}^*)$, $A\mathbf{u}^* = \mathbf{b}$ (as $A\mathbf{u}^{(k_j)} = \mathbf{b}$), and $D\mathbf{u}^* = \mathbf{h}^*$ (by the update of \mathbf{g}). It further follows from Lemma 2 that $\mathbf{0} \in \mathcal{L}(\mathbf{u}^*, \mathbf{h}^*, \mathbf{g}^*)$ and hence $(\mathbf{u}^*, \mathbf{h}^*)$ is a critical point of (11). \square

Theorem 3. (subsequential convergence of an inexact scheme) *Under Assumption 1 and a sufficiently large ρ , one can solve the \mathbf{u} -subproblem in (14) within an error tolerance ε_k , i.e.,*

$$\|\tilde{\mathbf{u}}^{(k+1)} - \mathbf{u}^{(k+1)}\|_2^2 \leq \varepsilon_k. \quad (29)$$

If $\sum_k \varepsilon_k < +\infty$, then the resulting sequence $\{\tilde{\mathbf{u}}^{(k)}, \mathbf{h}^{(k)}\}$ has a subsequence convergent to a critical point of (11).

6. Experimental results

In this section, we test the proposed algorithm on three prototypical imaging applications: super-resolution, MRI reconstruction, and limited-angle CT reconstruction. As analogous to Section 3, super-resolution refers to recovering a 2D image from low-frequency measurements, i.e., we restrict the data within a square in the center of the frequency domain. The data measurements for the MRI reconstruction are taken along radical lines in the frequency domain; such a radical pattern [40] is referred to as a mask. The sensing matrix for the CT reconstruction is the Radon transform [41], while the term ‘‘limited-angle’’ means the rotating angle does not cover the entire circle [42, 43, 44].

We evaluate the performance in terms of the relative error (RE) and the overall structural similarity index (SSIM) [45]. Here RE is defined as

$$\text{RE}(\mathbf{u}^*, \tilde{\mathbf{u}}) := \frac{\|\mathbf{u}^* - \tilde{\mathbf{u}}\|_2}{\|\tilde{\mathbf{u}}\|_2},$$

where \mathbf{u}^* is the restored image and $\tilde{\mathbf{u}}$ is the ground truth. SSIM is the mean of local similarity indices,

$$\text{SSIM}(\mathbf{u}^*, \tilde{\mathbf{u}}) := \frac{1}{N} \sum_{i=1}^N \text{ssim}(x_i, y_i),$$

where x_i, y_i are corresponding the i -th 8×8 windows for \mathbf{u}^* and $\tilde{\mathbf{u}}$, respectively, and N is the number of such windows. The local similarity index is defined as

$$\text{ssim}(x, y) := \frac{(2\mu_x\mu_y + c_1)(2\sigma_{xy} + c_2)}{(\mu_x^2 + \mu_y^2 + c_1)(\sigma_x^2 + \sigma_y^2 + c_2)}.$$

Here the averages/variances of x, y are denoted as μ_x/σ_x^2 and μ_y/σ_y^2 , respectively. The corresponding variances are σ_x^2 and σ_y^2 , where c_1 and c_2 are two fixed constants to avoid dividing by zero. We choose $c_1 = c_2 = 0.05$.

To ease with parameter tuning, we scale the pixel value to $[0, 1]$ for the original images in each application and rescale the solution back after computation. Hence the box constraint is set as $[0, 1]$. We start by discussing some algorithmic behaviors regarding the box constraint, the maximum number of inner iterations, and sensitivity analysis on algorithmic parameters in Section 6.1. The remaining sections are organized by specific applications. We compare the proposed L_1/L_2 approach with two regularization methods based on L_1 [1] and $L_1-\alpha L_2$ for $\alpha = 1/2$ as suggested in [27]. To have a fair comparison, we incorporate the $[0, 1]$ box constraint in L_1 , $L_1-\alpha L_2$, and L_1/L_2 models. We implement all these competing methods by ourselves and tune the parameters to achieve the smallest RE to the ground-truth. Due to the constrained formulation, no noise is added. We set the initial condition of \mathbf{u} to be a zero vector for all the methods. The stopping criterion for the proposed Algorithm 1 is when the relative error between two consecutive iterates is smaller than $\epsilon = 10^{-5}$ for both inner and outer iterations. All the numerical experiments are carried out in a desktop with CPU (Intel i7-9700F, 3.00 GHz) and MATLAB 9.8 (R2020a).

6.1. Algorithmic behaviors

We discuss three computational aspects of the proposed Algorithm 1. In particular, we want to analyze the influence of the box constraint, the maximum number of inner iterations (denoted by $jMax$), and the algorithmic parameters on the reconstruction results of MRI and CT problems. We use MATLAB's built-in function `phantom`, which is called the Shepp-Logan (SL) phantom, to test on 6 radial lines for MRI and 45° scanning range for CT. The analysis is assessed in terms of objective values $\frac{\|D\mathbf{u}^{(k)}\|_1}{\|D\mathbf{u}^{(k)}\|_2}$ and $RE(\mathbf{u}^{(k)}, \tilde{\mathbf{u}})$ versus the CPU time.

In Figure 5, we present algorithmic behaviors of the box constraint for both MRI and CT problems, in which we set $jMax$ to be 5 and 1, respectively (we will discuss the effects of inner iteration number shortly.) In the MRI problem, the box constraint is critical; without it, our algorithm converges to another local minimizer, as RE goes up. With the box constraint, the objective values decrease faster than in the no-box case, and the relative errors drop down monotonically. In the CT case, the influence of box is minor but we can see a faster decay of RE than the no-box case after 200 seconds. In the light of these observations, we only consider the algorithm with a box constraint for the rest of the experiments.

We then study the effect of $jMax$ on MRI/CT reconstruction problems in Figure 6. We fix the maximum outer iterations as 300, and examine four possible $jMax$ values: 1, 3, 5 and 10. In the case of MRI, $jMax = 10$ causes the slowest decay of both objective value and RE. Besides, we observe that only one inner iteration, which is equivalent to our previous approach [18], is not as efficient as more inner iterations to reduce the RE in the MRI problem. The CT results are slightly different, as one inner iteration seems sufficient to yield satisfactory results. The disparate behavior of CT to MRI is probably due to inexact solutions by CG iterations. In other words, more inner iterations do not

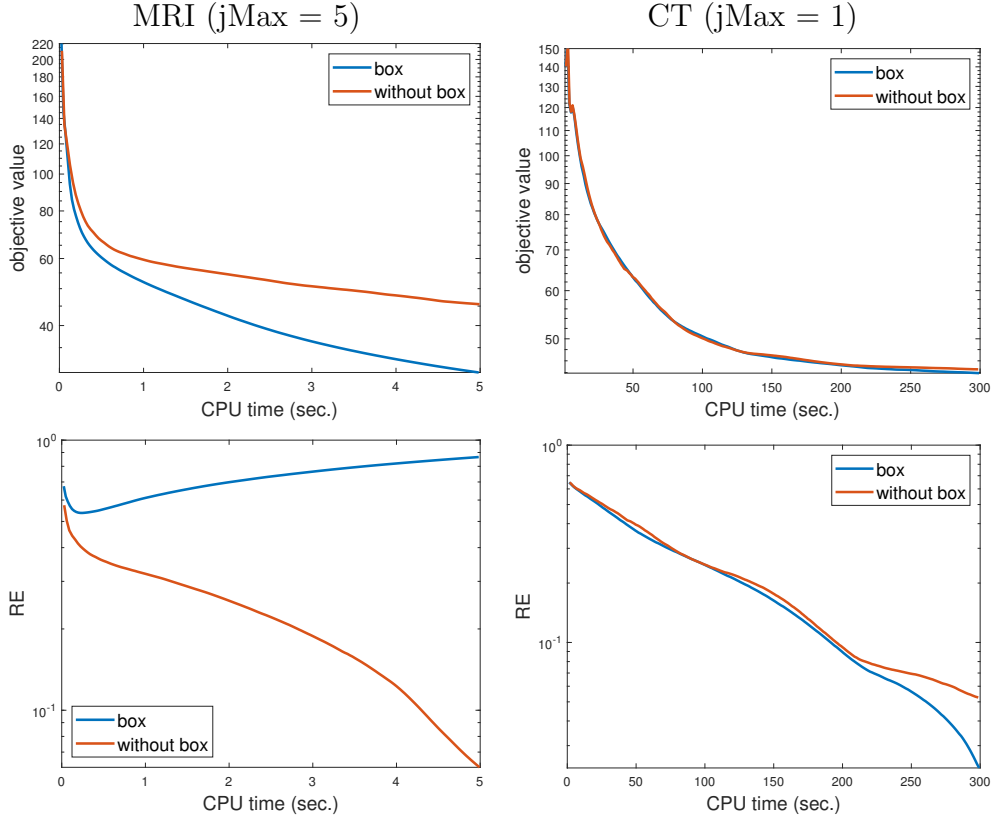


Figure 5. The effects of box constraint on objective values (top) and relative errors (bottom) for MRI (left) and CT (right) reconstruction problems.

improve the accuracy. Following Figure 6, we set $j\text{Max}$ to be 5 and 1 in MRI and CT, respectively, for the rest of the experiments.

Lastly, we study the sensitivity of the parameters λ, ρ, β in our proposed algorithm to provide strategies for parameter selection. For simplicity, we set $\gamma = \rho$ as their corresponding auxiliary variables represent $D\mathbf{u}$. In the MRI reconstruction problem, we examine three values of $\lambda \in \{100, 1000, 10000\}$ and two settings of the number of maximum outer iterations, i.e., $k\text{Max} \in \{500, 1000\}$. For each combination of λ and $k\text{Max}$, we vary parameters $(\rho, \beta) \in (2^i, 2^j)$, for $i, j = -2, -1, \dots, 3, 4$, and plot the RE in Figure 7. We observe that small values of ρ work well in practice, although we need to assume a sufficiently large value for ρ when proving the convergence results in Theorems 2 and 3. Besides, a larger $k\text{Max}$ value leads to larger valley regions for the lowest RE, which verifies that only ρ and β affect the convergence rate. Figure 7 suggests that our algorithm is generally insensitive to all these parameters β, ρ and λ as long as ρ is small. Similarly in the CT reconstruction, we set $\lambda \in \{0.005, 0.05, 0.5\}$, $k\text{Max} \in \{100, 300\}$, and $(\rho, \beta) \in (2^i, 2^j)$, for $i, j = -2, -1, \dots, 3, 4$. Figure 8 shows that ρ and β can be selected in a wide range, especially for large number of outer iterations. But our algorithm is sensitive to λ for the CT problem, as $\lambda = 0.005$ or 0.5 yields larger errors than $\lambda = 0.05$. In the light of this sensitivity analysis, we can tune parameters by

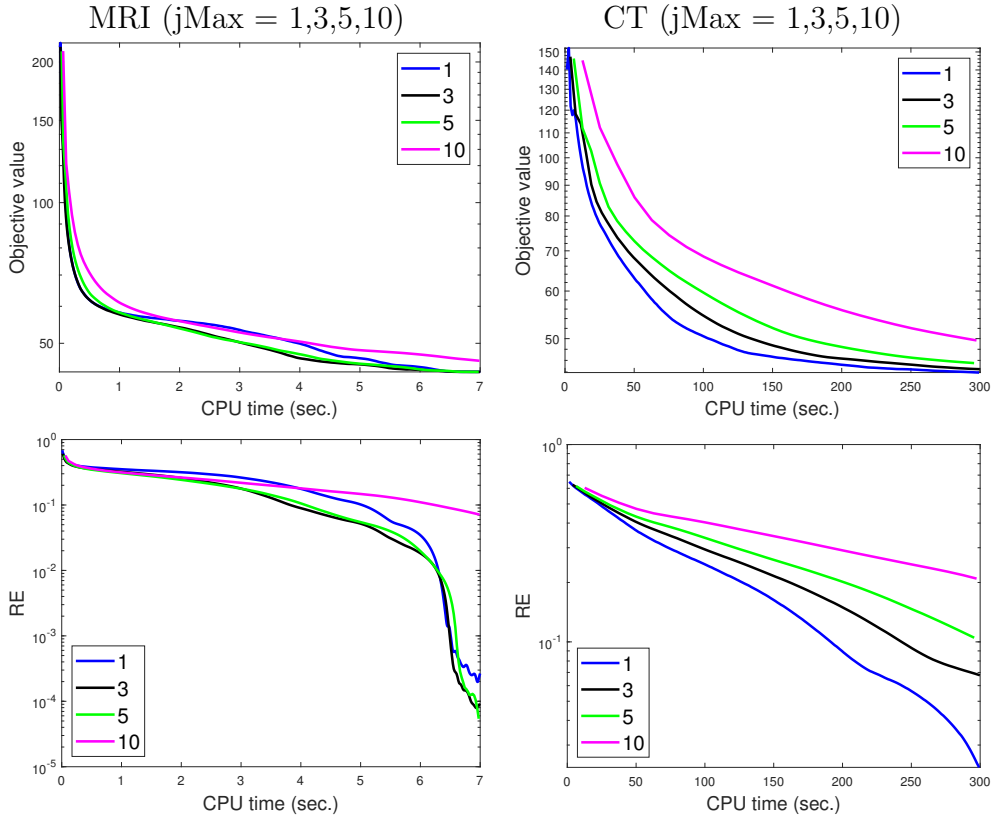


Figure 6. The effects of the maximum number in the inner loops (jMax) on objective values (top) and relative errors (bottom) for MRI (left) and CT (right) reconstruction problems.

finding the optimal combination among a candidate set for each problem, specifically paying attention to the value of λ in the limited-angle CT reconstruction.

6.2. Super-resolution

We use an original image from [46] of size 688×688 to illustrate the performance of super-resolution. As super-resolution is similar to MRI in the sense of frequency measurements, we set up the maximum iteration number as 5 according to Section 6.1. We restrict the data within a square in the center of the frequency domain (corresponding to low-frequency measurements), and hence varying the sizes of the square leads to different sampling ratios. In addition to regularized methods, we include a direct method of filling in the unknown frequency data by zero, followed by inverse Fourier transform, which is referred to as zero-filling (ZF). The visual results of 1% are presented in Figure 9, showing that L_1/L_2 is superior over ZF, L_1 , and $L_1-\alpha L_2$. Specifically, L_1/L_2 can recover these thin rectangular bars, while L_1 and $L_1-\alpha L_2$ lead to thicker bars with white background, which should be gray. In addition, L_1/L_2 can recover the most of the letter 'a' in the bottom of the image, compared to the other methods. One drawback of L_1/L_2 is that it produces white artifacts near the third square from the left

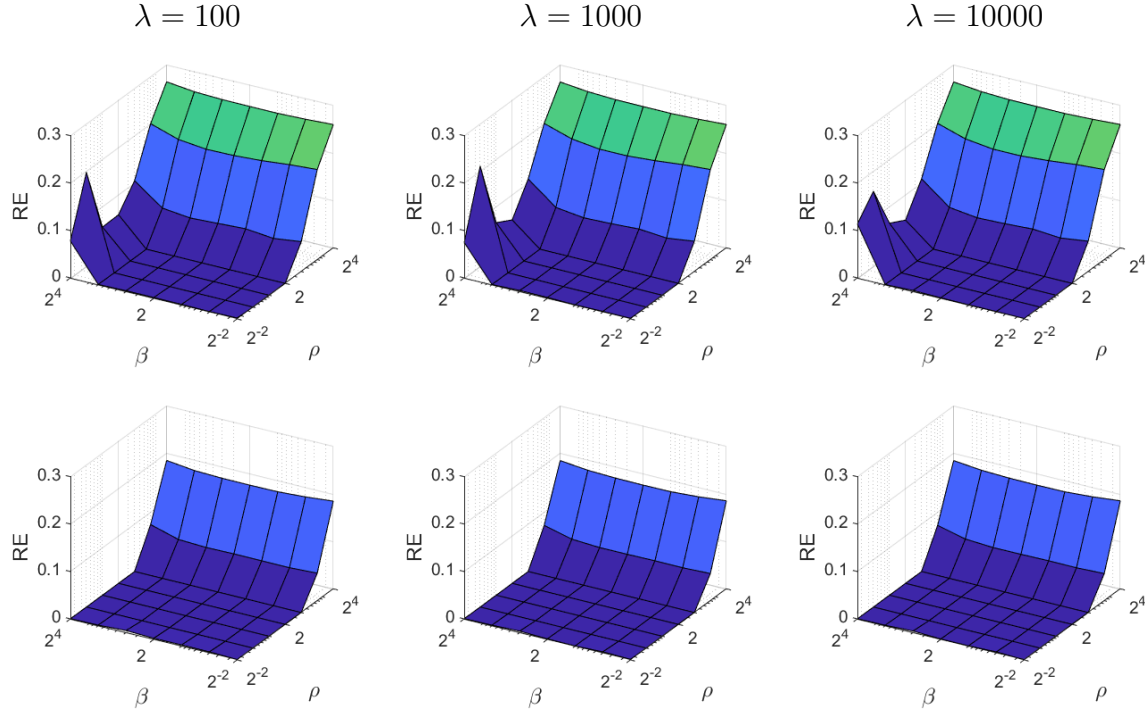


Figure 7. The relative errors with respect to the parameters λ, ρ, β in Algorithm 1 for MRI reconstruction when k_{Max} is 500 (top) or 1000 (bottom).

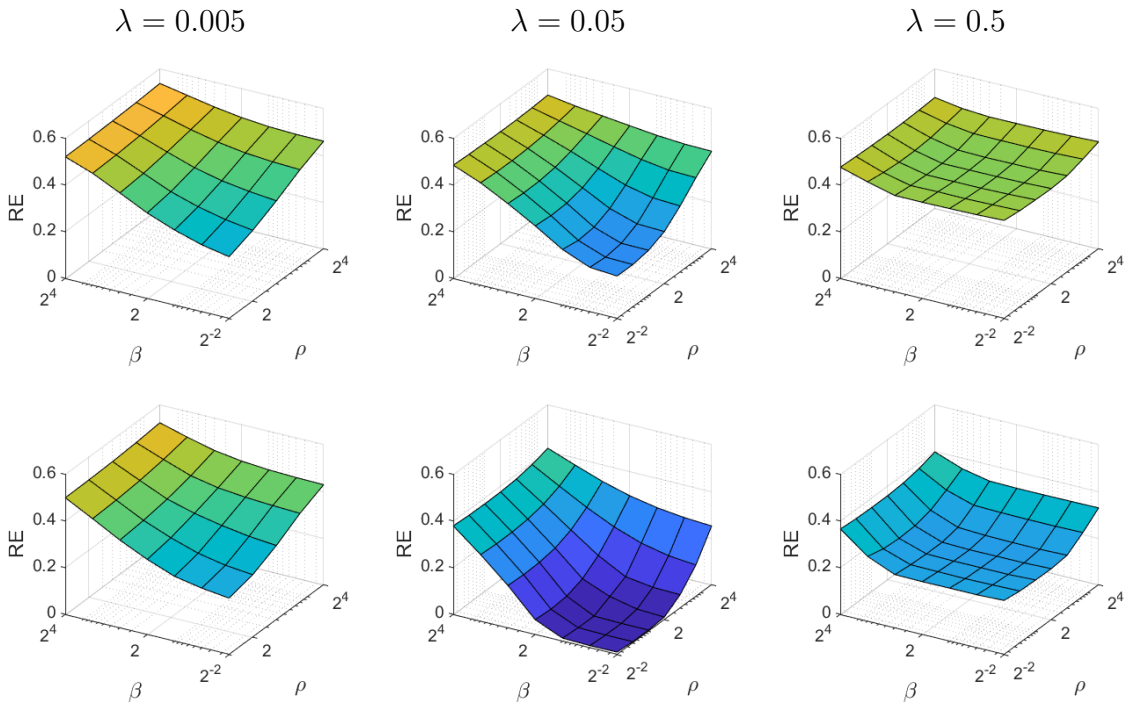


Figure 8. The relative errors with respect to the parameters λ, ρ, β in Algorithm 1 for CT reconstruction when k_{Max} is 100 (top) or 300 (bottom).

as well as around the letter ‘a’ in the middle. We suspect L_1/L_2 is not very stable, and the box constraint forces the black-and-white regions near edges. We do not present quantitative measures for this example, as four noisy squares on the right of the image lead to meaningless comparison, considering that all the methods return smooth results.

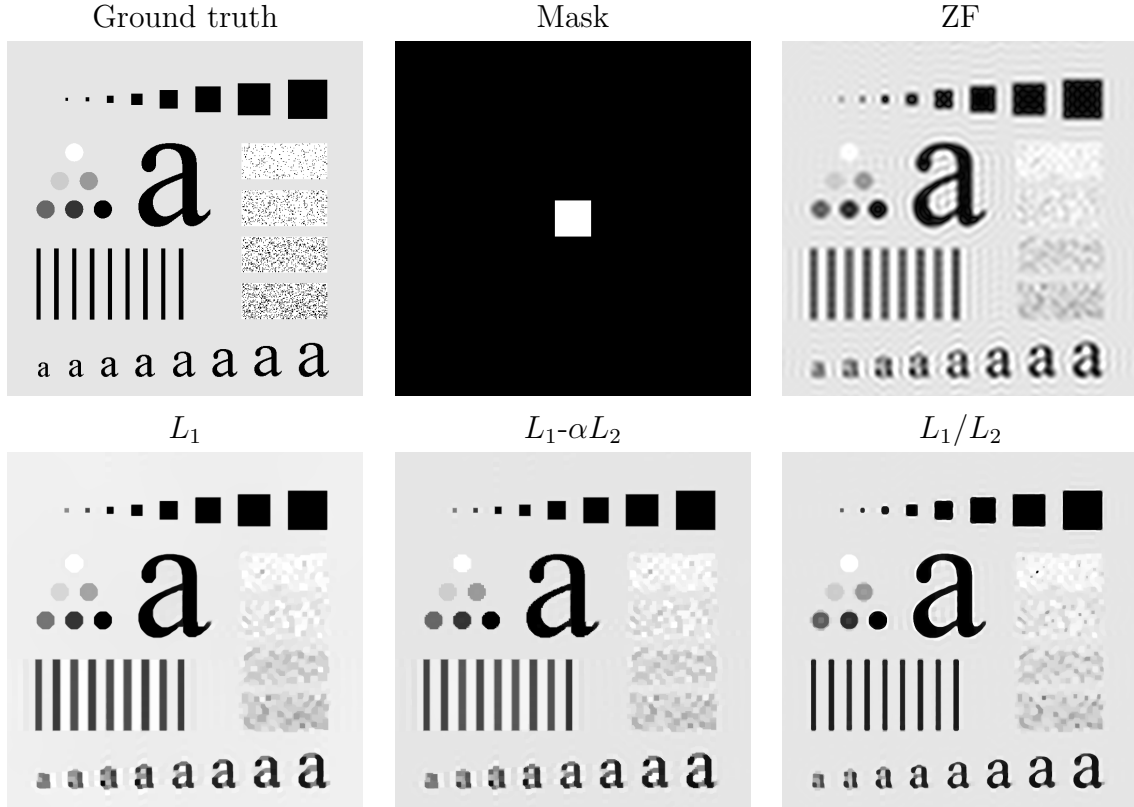


Figure 9. Super-resolution from 1% low frequency data.

6.3. MRI reconstruction

To generate the ground-truth MRI images, we utilize a simulated brain database [47, 48] that has full three-dimensional data volumes obtained by an MRI simulator [49] in different modalities such as T1 and T2 weighted images. As a proof of concept, we extract one slice from the 3D T1 and T2 data as testing images and take frequency data along radical lines. The visual comparisons are presented for 25 radical lines (about 13.74% measurements) in Figure 10. We include the zero-filled method as mentioned in super-resolution, which unfortunately fails to recover the contrast for both T1 and T2. The other regularization methods yield more blurred results than the proposed L_1/L_2 approach. Particularly worth noticing is that our proposed model can effectively separate the gray matter and white matter in the T1 image, as highlighted in the zoom-in regions. Furthermore, we plot the horizontal and vertical profiles in Figure 11, where we can see clearly that the restored profiles via L_1/L_2 are closer to the ground truth

Table 1. MRI reconstruction from different numbers of radical lines.

Image	Line	ZF		L_1		$L_1-\alpha L_2$		L_1/L_2	
		SSIM	RE	SSIM	RE	SSIM	RE	SSIM	RE
T1	20	0.64	22.13%	0.90	11.17%	0.91	10.90%	0.95	7.92%
	25	0.73	17.26%	0.95	7.80%	0.95	7.78%	0.98	5.40%
	30	0.74	16.02%	0.97	6.48%	0.96	6.65%	0.98	4.40%
T2	20	0.51	33.91%	0.78	23.37%	0.81	21.75%	0.88	17.19%
	25	0.57	30.44%	0.86	18.99%	0.88	17.58%	0.93	13.12%
	30	0.61	28.43%	0.89	16.26%	0.91	14.78%	0.95	10.69%

than the other approaches, especially near these peaks that can be reached by $L_1-\alpha L_2$ and L_1/L_2 , but not L_1 . As a further comparison, we present the MRI reconstruction results under various number of lines (20, 25, and 30) in Table 1, which demonstrates significant improvements of L_1/L_2 over the other models in term of SSIM and RE.

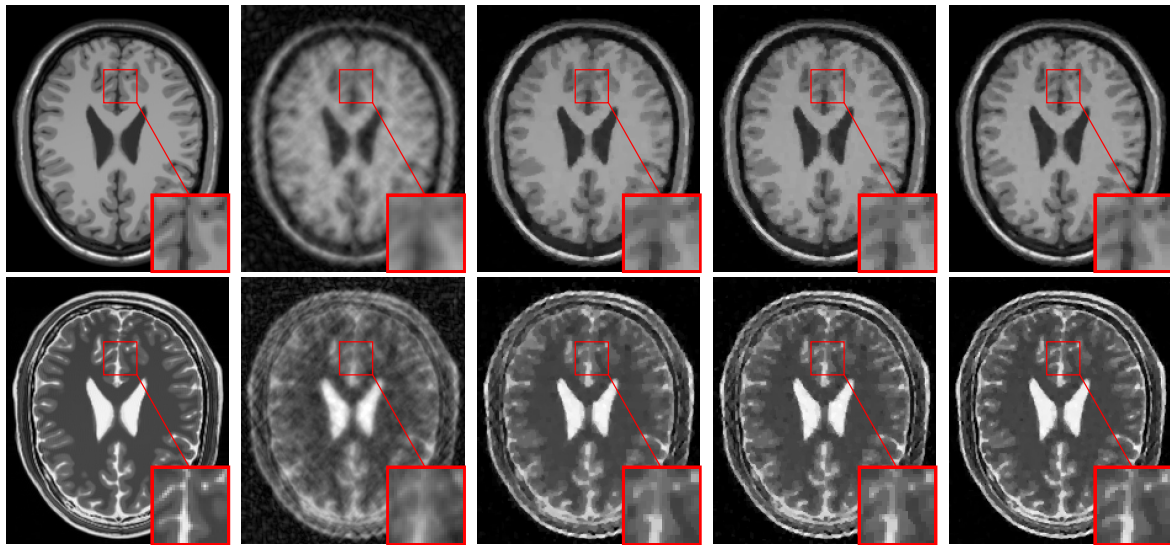


Figure 10. MRI reconstruction from frequency measurements along 25 radical lines of T1 (top row) and T2 (bottom row). From left to right: ground truth, ZF, L_1 , $L_1-\alpha L_2$, and L_1/L_2 .

6.4. Limited-angle CT reconstruction

Lastly, we examine the limited-angle CT reconstruction problem on two standard phantoms: Shepp-Logan (SL) by Matlab's built-in command (`phantom`) and FORBILD (FB) [50]. Notice that the FB phantom has a very low image contrast and we display it with the grayscale window of [1.0, 1.2] in order to reveal its structures; see Figure 12. To synthesize the CT projected data, we discretize both phantoms at a resolution of 256×256 . The forward operator A is generated as the discrete Radon transform with a parallel beam geometry sampled at $\theta_{\text{Max}}/30$ over a range of θ_{Max} , resulting in a sub-

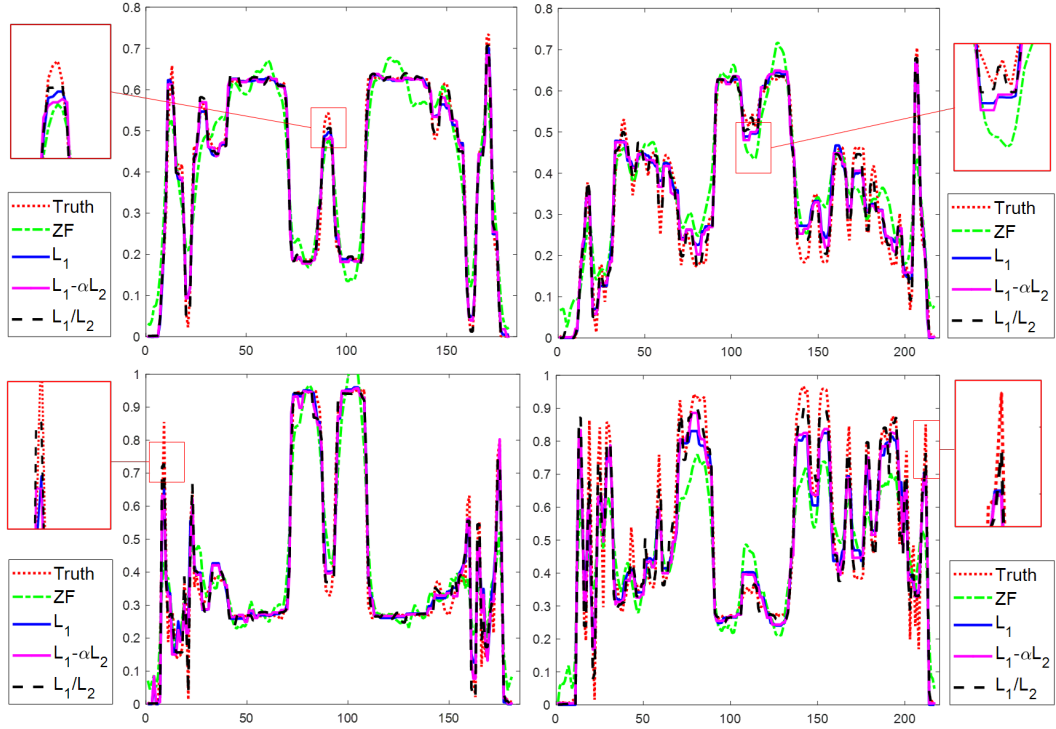


Figure 11. Horizontal (top) and vertical (bottom) profiles of MRI reconstruction results from 25 radical lines for T1 (left) and T2 (right).

sampled data of size 362×31 . Note that we use the same number of projections when we vary ranges of projection angles. The simulation process is available in the IR and AIR toolbox [51, 52]. Following the discussion in Section 6.1, we set $jMax=1$ for the subproblem. We compare the regularization models with a clinical standard approach, called simultaneous algebraic reconstruction technique (SART) [53].

As the SL phantom has relatively simpler structures than FB, we present an extremely limited angle of only 30° scanning range in Table 2, which shows that L_1/L_2 achieves perfect SSIM scores and significant improvements over SART, L_1 , and $L_1-\alpha L_2$ in terms of SSIM and RE. Visually, we present the CT reconstruction results of 45° projection range for SL (SL- 45°) and 75° for FB (FB- 75°) in Figure 12. In the first case (SL- 45°), SART fails to recover the ellipse inside of the skull with such a small range of projection angles. All the regularization methods perform much better owing to their sparsity promoting property. However, the L_1 model is unable to restore the bottom skull and preserve details of some ellipses in the middle. The proposed L_1/L_2 method leads an almost exact recovery with a relative error of 0.64% and visually no difference to the ground truth. In the second case (FB- 75°), we show the reconstructed images with the window of $[1.0, 1.2]$, and observe some fluctuations inside of the skull. None of the methods seems to produce satisfactory results under such a narrow display window, but L_1/L_2 achieves the perfect SSIM score of 1 and restores the most details of

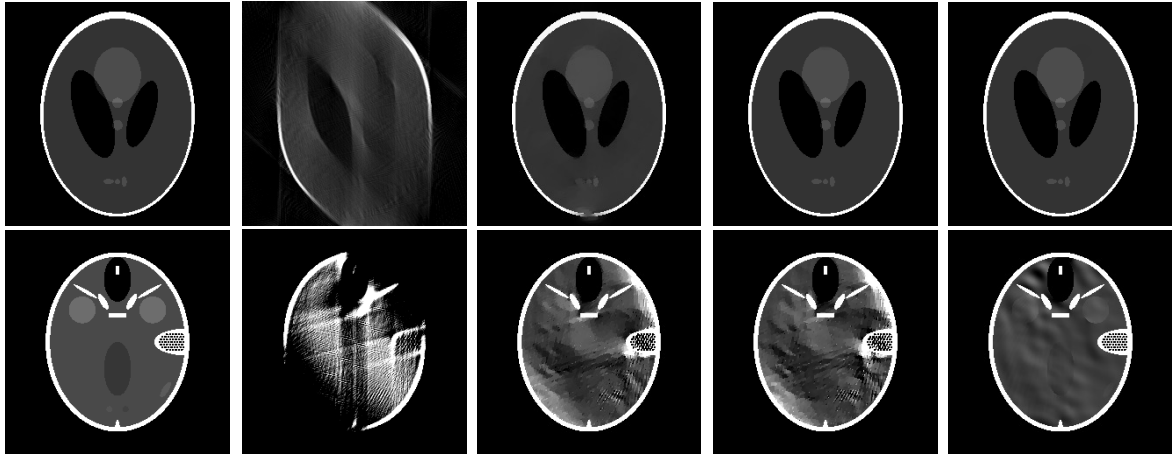


Figure 12. CT reconstruction results of SL-45° (top) and FB-75° (bottom). From left to right: ground truth, SART, L_1 , $L_1-\alpha L_2$, and L_1/L_2 . The gray scale window is $[0, 1]$ for SL and $[1, 1.2]$ for FB.

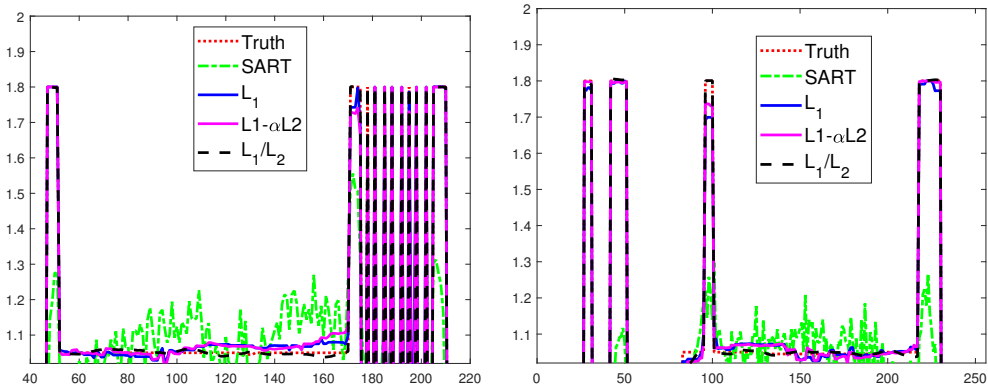


Figure 13. Horizontal and vertical profiles of CT reconstruction results of FB-75°.

the image among the competing methods. We plot the horizontal and vertical profiles in Figure 13, which illustrates that L_1/L_2 leads to the smallest fluctuations compared to the other methods. We also observe a well-known artifact of the L_1 method, i.e., loss-of-contrast, as its profile fails to reach the height of jump on the intervals such as $[160, 180]$ in the left plot and $[220, 230]$ in the right plot of Figure 13, while L_1/L_2 has a good recovery in these regions.

7. Conclusions and future works

In this paper, we considered the use of L_1/L_2 on the gradient as an objective function to promote sparse gradients for imaging problems. We started from a series of 1D piecewise signal recovery and demonstrated the superiority of the ratio model over L_1 , which is widely known as the total variation. To facilitate the discussion on the empirical evidences, we focused on a constrained model, and proposed a splitting

Table 2. CT reconstruction with difference ranges of scanning angles.

phantom	range	SART		L_1		$L_1-\alpha L_2$		L_1/L_2	
		SSIM	RE	SSIM	RE	SSIM	RE	SSIM	RE
SL	30°	0.59	66.95%	0.98	15.60%	0.99	5.02%	1.00	0.64%
	45°	0.61	63.78%	0.99	8.75%	1.00	0.28%	1.00	2.65%
	60°	0.59	66.95%	1.00	2.75%	1.00	0.04%	1.00	0.15%
FB	60°	0.39	40.16%	0.96	12.96%	0.96	11.81%	1.00	1.09%
	75°	0.48	37.79%	0.99	8.76%	0.98	8.13%	1.00	0.83%
	90°	0.50	35.68%	1.00	0.08%	1.00	0.04%	1.00	0.07%

algorithm scheme that has provable convergence for ADMM. We conducted extensive experiments to demonstrate that our approach outperforms the state-of-the-art gradient-based approaches. Motivated by the empirical studies in Section 3, we will devote ourselves to the exact recovery of the TV regularization with respect to the minimum separation of the gradient spikes. We are also interested in extending the analysis to the unconstrained formulation, which is widely applicable in image processing.

Acknowledgments

C. Wang was partially supported by HKRGC Grant No. CityU11301120 and NSF CCF HDR TRIPDS grant 1934568. M. Tao was supported in part by the Natural Science Foundation of China (No. 11971228) and the Jiangsu Provincial National Natural Science Foundation of China (No. BK20181257). C-N. Chuah was partially supported by NSF CCF HDR TRIPDS grant 1934568. J. Nagy was partially supported by NSF DMS-1819042 and NIH 5R01CA181171-04. Y. Lou was partially supported by NSF grant CAREER 1846690.

References

- [1] Rudin L, Osher S, Fatemi E. Nonlinear total variation based noise removal algorithms. *Physica D*. 1992;60:259–268.
- [2] Bredies K, Kunisch K, Pock T. Total generalized variation. *SIAM J Imaging Sci*. 2010;3(3):492–526.
- [3] Chen D, Chen YQ, Xue D. Fractional-order total variation image denoising based on proximity algorithm. *Appl Math Comput*. 2015;257(1):537–545.
- [4] Zhang J, Chen K. A total fractional-Order variation model for image restoration with nonhomogeneous boundary conditions and its numerical solution. *SIAM J Imaging Sci*. 2015;8(4):2487–2518.
- [5] Osher SJ, Esedoglu S. Decomposition of images by the anisotropic Rudin-Osher-Fatemi model. *Comm Pure Appl Math*. 2003;57:1609–1626.
- [6] Natarajan BK. Sparse approximate solutions to linear systems. *SIAM J Comput*. 1995;p. 227–234.
- [7] Candès EJ, Romberg J, Tao T. Stable signal recovery from incomplete and inaccurate measurements. *Comm Pure Appl Math*. 2006;59:1207–1223.
- [8] Fan J, Li R. Variable selection via nonconcave penalized likelihood and its oracle properties. *J Am Stat Assoc*. 2001;96(456):1348–1360.

- [9] Zhang C. Nearly unbiased variable selection under minimax concave penalty. *Ann Stat.* 2010;p. 894–942.
- [10] Zhang T. Multi-stage convex relaxation for learning with sparse regularization. In: *Adv. Neural. Inf. Process. Syst.*; 2009. p. 1929–1936.
- [11] Shen X, Pan W, Zhu Y. Likelihood-based selection and sharp parameter estimation. *J Am Stat Assoc.* 2012;107(497):223–232.
- [12] Lou Y, Yin P, Xin J. Point source super-resolution via non-convex L_1 based methods. *J Sci Comput.* 2016;68:1082–1100.
- [13] Lv J, Fan Y. A unified approach to model selection and sparse recovery using regularized least squares. *Ann Appl Stat.* 2009;p. 3498–3528.
- [14] Zhang S, Xin J. Minimization of transformed L_1 penalty: closed form representation and iterative thresholding algorithms. *Comm Math Sci.* 2017;15:511–537.
- [15] Zhang S, Xin J. Minimization of transformed L_1 penalty: theory, difference of convex function algorithm, and robust application in compressed sensing. *Math Program.* 2018;169:307–336.
- [16] Chartrand R. Exact reconstruction of sparse signals via nonconvex minimization. *IEEE Signal Process Lett.* 2007;10(14):707–710.
- [17] You J, Jiao Y, Lu X, Zeng T. A nonconvex model with minimax concave penalty for image restoration. *J Sci Comput.* 2019;78(2):1063–1086.
- [18] Rahimi Y, Wang C, Dong H, Lou Y. A scale invariant approach for sparse signal recovery. *SIAM J Sci Comput.* 2019;41(6):A3649–A3672.
- [19] Wang C, Yan M, Rahimi Y, Lou Y. Accelerated schemes for the L_1/L_2 minimization. *IEEE Trans Signal Process.* 2020;68:2660–2669.
- [20] Tao M, Lou Y. Minimization of L1 over L2 for sparse signal recovery with convergence guarantee; 2020. http://www.optimization-online.org/DB_HTML/2020/10/8064.html.
- [21] Candès EJ, Eldar YC, Needell D, Randall P. Compressed sensing with coherent and redundant dictionaries. *Appl Comput Harmon Anal.* 2011;31(1):59–73.
- [22] Needell D, Ward R. Stable image reconstruction using total variation minimization. *SIAM J Imaging Sci.* 2013;6(2):1035–1058.
- [23] Tillmann AM, Pfetsch ME. The computational complexity of the restricted isometry property, the nullspace property, and related concepts in compressed sensing. *IEEE Trans Inf Theory.* 2013;60(2):1248–1259.
- [24] Candès EJ, Fernandez-Granda C. Super-resolution from noisy data. *J Fourier Anal Appl.* 2013;19(6):1229–1254.
- [25] Wang C, Tao M, Nagy J, Lou Y. Limited-angle CT reconstruction via the L_1/L_2 minimization. arXiv preprint arXiv:200600601. 2020;.
- [26] Boyd S, Parikh N, Chu E, Peleato B, Eckstein J. Distributed optimization and statistical learning via the alternating direction method of multipliers. *Found Trends Mach Learn.* 2011 Jan;3(1):1–122.
- [27] Lou Y, Zeng T, Osher S, Xin J. A weighted difference of anisotropic and isotropic total variation model for image processing. *SIAM J Imaging Sci.* 2015;8(3):1798–1823.
- [28] Yin P, Ecker E, Xin J. Ratio and Difference of l_1 and l_2 Norms and Sparse Representation with Coherent Dictionaries. *Comm Info Systems.* 2014;14:87–109.
- [29] Lou Y, Yin P, He Q, Xin J. Computing sparse representation in a highly coherent dictionary based on difference of L_1 and L_2 . *J Sci Comput.* 2015;64(1):178–196.
- [30] Ma T, Lou Y, Huang T. Truncated L_1 - L_2 models for sparse recovery and rank minimization. *SIAM J Imaging Sci.* 2017;10(3):1346–1380.
- [31] Lou Y, Yan M. Fast L_1 - L_2 minimization via a proximal operator. *J Sci Comput.* 2018;74(2):767–785.
- [32] Guo K, Han D, Wu T. Convergence of alternating direction method for minimizing sum of two nonconvex functions with linear constraints. *Int J of Comput Math.* 2017;94(8):1653–1669.
- [33] Pang JS, Tao M. Decomposition methods for computing directional stationary solutions of a class

- of nonsmooth nonconvex optimization problems. *SIAM J Optim.* 2018;28(2):1640–1669.
- [34] Wang Y, Yin W, Zeng J. Global convergence of ADMM in nonconvex nonsmooth optimization. *J Sci Comput.* 2019;78(1):29–63.
 - [35] Candès EJ, Fernandez-Granda C. Towards a mathematical theory of super-resolution. *Comm Pure Appl Math.* 2014;67(6):906–956.
 - [36] Grant M, Boyd S. CVX: Matlab Software for Disciplined Convex Programming, version 2.1; 2014. <http://cvxr.com/cvx>.
 - [37] Chan RH, Ma J. A multiplicative iterative algorithm for box-constrained penalized likelihood image restoration. *IEEE Trans Image Process.* 2012;21(7):3168–3181.
 - [38] Kan K, Fung SW, Ruthotto L. PNKH-B: A Projected Newton-Krylov Method for Large-Scale Bound-Constrained Optimization. *arXiv preprint arXiv:200513639.* 2020;.
 - [39] Nocedal J, Wright SJ. *Numerical Optimization.* Springer; 2006.
 - [40] Candès EJ, Romberg J, Tao T. Robust uncertainty principles: Exact signal reconstruction from highly incomplete frequency information. *IEEE Trans Inf Theory.* 2006;52(2):489–509.
 - [41] Avinash C, Malcolm S. *Principles of computerized tomographic imaging.* Philadelphia, PA, USA: Society for Industrial and Applied Mathematics; 2001.
 - [42] Chen Z, Jin X, Li L, Wang G. A limited-angle CT reconstruction method based on anisotropic TV minimization. *Phys Med Biol.* 2013;58(7):2119.
 - [43] Zhang Y, Chan HP, Sahiner B, Wei J, Goodsitt MM, Hadjiiski LM, et al. A comparative study of limited-angle cone-beam reconstruction methods for breast tomosynthesis. *Med Phys.* 2006;33(10):3781–3795.
 - [44] Wang Z, Huang Z, Chen Z, Zhang L, Jiang X, Kang K, et al. Low-dose multiple-information retrieval algorithm for X-ray grating-based imaging. *Nucl Instrum Methods Phys.* 2011;635(1):103–107.
 - [45] Wang Z, Bovik AC, Sheikh HR, Simoncelli EP. Image quality assessment: From error visibility to structural similarity. *IEEE Trans on Image Process.* 2004 April;13(4):600–612.
 - [46] Gonzalez RC, Woods RE, Eddins SL. *Digital image processing using MATLAB.* Pearson Education India; 2004.
 - [47] Cocosco CA, Kollokian V, Kwan RKS, Pike GB, Evans AC. BrainWeb: Online Interface to a 3D MRI Simulated Brain Database. *NeuroImage.* 1997;5:425.
 - [48] Kwan RS, Evans AC, Pike GB. MRI simulation-based evaluation of image-processing and classification methods. *IEEE Trans Med Imaging.* 1999;18(11):1085–1097.
 - [49] Kwan RKS, Evans AC, Pike GB. An extensible MRI simulator for post-processing evaluation. In: *International Conference on Visualization in Biomedical Computing.* Springer; 1996. p. 135–140.
 - [50] Yu Z, Noo F, Dennerlein F, Wunderlich A, Lauritsch G, Hornegger J. Simulation tools for two-dimensional experiments in x-ray computed tomography using the FORBILD head phantom. *Phys Med Biol.* 2012;57(13):N237.
 - [51] Gazzola S, Hansen PC, Nagy JG. IR Tools: a MATLAB package of iterative regularization methods and large-scale test problems. *Numer Algorithms.* 2019;81(3):773–811.
 - [52] Hansen PC, Saxild-Hansen M. AIR tools — MATLAB package of algebraic iterative reconstruction methods. *J Comput Appl Math.* 2012;236(8):2167–2178.
 - [53] Andersen AH, Kak AC. Simultaneous algebraic reconstruction technique (SART): a superior implementation of the ART algorithm. *Ultrason Imaging.* 1984;6(1):81–94.